Journal of Power Sources 195 (2010) 6782–6794

Contents lists available at ScienceDirect

Journal of Power Sources

journal homepage: www.elsevier.com/locate/jpowsour

Parametric study of the cathode and the role of liquid saturation on the performance of a polymer electrolyte membrane fuel cell—A numerical approach

M. Srinivasarao[a], D. Bhattacharyya[b], R. Rengaswamy[c,d,*], S. Narasimhan[a]

[a] Department of Chemical Engineering, IIT Madras, India
[b] Department of Chemical Engineering, West Virginia University, Morgantown, USA
[c] Department of Chemical Engineering, Texas Tech University, Lubbock, TX 79409, USA
[d] Department of Chemical and Bio-Molecular Engineering, Clarkson University, Potsdam, NY 13699, USA

ARTICLE INFO

Article history:
Received 22 December 2009
Received in revised form 2 March 2010
Accepted 2 March 2010
Available online 7 March 2010

Keywords:
PEMFC
Water management
Interface saturation
Two layer diffusion medium
Capillary pressure
Parametric studies

ABSTRACT

A two-dimensional two-phase steady state model of the cathode of a polymer electrolyte membrane fuel cell (PEMFC) is developed using unsaturated flow theory (UFT). A gas flow field, a gas diffusion layer (GDL), a microporous layers (MPL), a finite catalyst layer (CL), and a polymer membrane constitute the model domain. The flow of liquid water in the cathode flow channel is assumed to take place in the form of a mist. The CL is modeled using flooded spherical agglomerate characterization. Liquid water is considered in all the porous layers. For liquid water transport in the membrane, electro-osmotic drag and back diffusion are considered to be the dominating mechanisms. The void fraction in the CL is expressed in terms of practically achievable design parameters such as platinum loading, Nafion loading, CL thickness, and fraction of platinum on carbon. A number of sensitivity studies are conducted with the developed model. The optimum operating temperature of the cell is found to be 80–85 °C. The optimum porosity of the GDL for this cell is in the range of 0.7–0.8. A study by varying the design parameters of the CL shows that the cell performs better with 0.3–0.35 mg cm^{-2} of platinum and 25–30 wt% of ionomer loading at high current densities. The sensitivity study shows that a multi-variable optimization study can significantly improve the cell performance. Numerical simulations are performed to study the dependence of capillary pressure on liquid saturation using various correlations. The impact of the interface saturation on the cell performance is studied. Under certain operating conditions and for certain combination of materials in the GDL and CL, it is found that the presence of a MPL can deteriorate the performance especially at high current density.

1. Introduction

PEM fuel cells (PEMFCs) are gaining importance because of their high potential for generating power at an affordable cost and high reliability. Prototypes of fuel cell vehicles and hybrid systems have already been tested successfully. However, in order to compete with internal combustion (IC) engines and battery vehicles, the cost needs to be reduced and the system performance should be improved. The performance of the cell mainly depends on the operating conditions, design of the flow field, composition and design parameters of the membrane electrode assembly (MEA), and the techniques used for preparing the MEA. To optimize the performance of the cell, it is necessary to have a better understanding of the various processes that take place inside the cell and also their influence on the cell performance. Quite often, it is expensive, time consuming, and difficult to study all these processes through experiments. Hence, a detailed mathematical model is needed to simulate various model parameters on the cell performance. A number of publications on the modeling of PEMFC can be found in the existing literature [1–17]. Some recent studies [18–21] have focused on water management and the effect of addition of a MPL to the GDL [22–24].

Even though transport of water through the polymer membrane is critical for good performance of the cell, very few models [1,7,12,13,16,25–29] in the open literature have considered this phenomenon. Excess water causes flooding which blocks the pores and hence reduces the cell performance. On the other hand, sufficient amount of water is required for the transport of protons through the membrane. Modeling the polymer membrane can help to capture the effect of liquid water as the current generated by the cell changes. In addition, as the capillary pressure, the difference between the gas and liquid pressures, plays a key role in the two-phase transport of water, the model should precisely capture

* Corresponding author. Tel.: +1 806 742 1765.
E-mail addresses: raghu.rengasamy@ttu.edu, raghu@clarkson.edu (R. Rengaswamy).

0378-7753/$ – see front matter © 2010 Elsevier B.V. All rights reserved.
doi:10.1016/j.jpowsour.2010.03.003

Nomenclature

a_a	Effective area of the catalyst layer per unit volume of the catalyst layer (m^2 Pt m^{-3})
a_{Pt}	Specific surface area of platinum (m^2 Pt (kg Pt)$^{-1}$)
a_{Pt}^{eff}	Effective surface area of the platinum (m^2 Pt (kg Pt)$^{-1}$)
a_{RL}	Area of cross section of the catalyst layer (m^2)
a_w	Activity of water inside the ionomer phase
a^{++}	Tuning parameter
c_f	Fixed charge site concentration (mol m^{-3})
C_i^k	Concentration of species i in region k (mol m^{-3})
$C_{i,o}$	Inlet concentrations of i (mol m^{-3})
C_W^{mem}	Concentration of liquid water in the membrane (mol m^{-3})
c_1, c_2, c_3	Constant capillary pressure gradients
$D_i^{eff,k}$	Effective diffusivity of the species i in region k (m^2 s^{-1})
$D_{O_2}^{mem}$	Diffusivity of oxygen in ionomer (m^2 s^{-1})
D_W^{mem}	Diffusivity of liquid water in the membrane (m^2 s^{-1})
E	Activation energy (J mol^{-1})
f_{area}	Fraction of area available for the reaction
$f_{ionomer}$	Weight fraction of ionomer in the catalyst layer
f_{Pt}	Weight fraction of platinum on carbon
F	Faraday's constant (C (g equiv.)$^{-1}$)
h	Brooks–Corey parameter
$H_{O_2}^{mem}$	Henry's constant for air–ionomer interface (atm m^3 mol^{-1})
$H_{O_2}^{W}$	Henry's constant for air–water interface (atm m^3 mol^{-1})
i_a	Local current density (A m^{-2})
i_{cell}	Cell current density (A m^{-2})
i_o	Exchange current density for oxygen reduction on platinum (A m^{-2} (kg Pt)$^{-1}$)
i_o^{ref}	Reference exchange current density for oxygen reduction on platinum (A m^{-2} (kg Pt)$^{-1}$)
J_i^k	Local flux due to diffusion of species i in region k (mol m^{-2} s^{-1})
k	Condensation constant (s^{-1})
k_v	Evaporation constant (atm^{-1} s^{-1})
$K_{wo,k}$	Permeability of liquid water inside porous region k at 100% saturation (m^2)
K_1, K_2, K_3	Constants for interface saturation
m	Van Genuchten parameter
m_{Pt}	Platinum loading inside the catalyst layer (kg Pt (m^2 CL)$^{-1}$)
n	Number of electrons taking part in the oxygen reduction reaction
n_d	Net electro-osmotic drag coefficient
$N_{W,k}$	Flux of liquid water in region k (mol m^{-2} s^{-1})
p_w	Partial pressure of water vapor (atm)
p^{sat}	Saturation pressure of water vapor (atm)
P_c	Capillary pressure (atm)
p_d	Entry pressure (Pa)
r_{agg}	Agglomerate radius (m)
R	Universal gas constant (J mol^{-1} K^{-1})
R_{O_2}	Rate of oxygen reduction reaction per unit volume of the catalyst layer (mol m^{-3} s^{-1})
R_w	Interfacial transfer of water between liquid and vapor (mol m^{-3} s^{-1})
s_k	Liquid water saturation level in region k
S_ϕ	Source term
t_{CL}	Thickness of the catalyst layer (m)
T_{air}	Cathode inlet air temperature (K)
T_{cell}	Cell temperature (K)
v_c	Volume occupied by the carbon inside catalyst layer (m^3)
v_{CL}	Volume of the catalyst layer (m^3)
$v_{ionomer}$	Volume occupied by the ionomer inside catalyst layer (m^3)
v_{Pt}	Volume occupied by the platinum inside catalyst layer (m^3)
v_s	Volume of solids inside catalyst layer (m^3)
v_V	Void volume inside catalyst layer (m^3)
V_{cell}	Cell voltage (V)
w_c	Mass of carbon inside the agglomerate (kg)
$w_{ionomer}$	Mass of ionomer inside the agglomerate (kg)
w_{Pt}	Mass of platinum inside the catalyst layer (kg)

Greek letters

α_a	Vapor activity in the gas phase in the anode catalyst layer
α_c	Vapor activity in the gas phase in the cathode catalyst layer
β	Cathode transfer coefficient
δ_{mem}	Thickness of the ionomer film covering the agglomerate (m)
δ_w	Thickness of the water layer on the top of the agglomerate (m)
ε_k	Void fraction inside region k
$\varepsilon_{ionomer}$	Fraction of volume occupied by the ionomer inside the catalyst layer
$\kappa^{eff,c}$	Effective proton conductivity in the catalyst layer (mho m^{-1})
$\kappa^{eff,mem}$	Effective proton conductivity in the membrane (mho m^{-1})
κ_{ele}^k	Electric conductivity in region k (S m^{-1})
$\kappa_{ele}^{eff,k}$	Effective electric conductivity in region k (S m^{-1})
λ_w	Water content in the membrane (mol H_2O (mol SO_3)$^{-1}$)
ρ_c	Density of carbon (kg m^{-3})
$\rho_{ionomer}$	Density of ionomer (kg m^{-3})
ρ_{Pt}	Density of platinum (kg m^{-3})
ρ_w	Density of water (kg m^{-3})
σ	Surface tension (N m^{-1})
θ_c	Contact angle

Subscripts

i	Index for the species: O_2, N_2, H_2O
k	Index for the region: diffusion layer, microporous layer, catalyst layer

the variation in the capillary pressure with change in the liquid saturation and wetting properties of the medium. A few experimental as well as simulation studies [23,30–32] have been performed on capillary pressure measurements with different perspectives. But, considerable debate still exists regarding the mechanism of water transport and the appropriate correlation of capillary pressure for a particular material. This paper addresses some of the key issues for the efficient operation of a PEMFC with a detailed two-dimensional two-phase model of the cathode and the polymer membrane.

A two-dimensional two-phase steady state model of a PEMFC cathode was developed previously by our group [17]. The results showed that the model with spherical agglomerate characteriza-

tion of the CL predicted the experimental data better than the model with macro-homogenous characterization. Though the effect of liquid water was considered in all the porous layers, the polymer membrane was excluded from the modeling domain by assuming negligible ionic resistance and no net transport of water through the membrane. The electronic resistance was also neglected [17]. The current work enhances our previous model by considering transport of water and proton through the polymer membrane and transport of electrons through the layers in the cathode. The objective is to use this model for sensitivity and optimization studies. The loss mechanisms considered in this paper can be insignificant in a specific operating condition for a particular cell (based on the cell geometry, dimensions, design parameters, materials of construction, etc.). However while doing sensitivity and optimization studies, the design parameters and the operating conditions are changed in a wide range and the model must be valid in that range. The intent of the model enhancement is to capture the cell performance in such optimization studies.

The developed model is validated with experimental data from Wang et al. [22]. The effect of the operating conditions, design parameters, and the model parameters on the cell performance is studied by utilizing the modified model. Finally, a water management study is presented considering various correlations for capillary pressure and showing the impact of the interfacial liquid saturation on the cell performance.

2. Model development

A two-dimensional two-phase steady state model is developed for the cathode of a PEMFC. The model also includes the polymer electrolyte membrane. The schematic of the cathode is shown in Fig. 1. The cathode gas flow field contains parallel channels of uniform cross section. It is assumed that the liquid water exists in the form of droplets and moves with the same velocity as the gaseous reactants. As air flows through these channels, it moves through the GDL and the MPL to reach the CL. The CL is modeled using a spherical agglomerate characterization. This characterization assumes that the CL consists of small agglomerates that are spherical in shape. The agglomerate is assumed to be covered by a thin film of ionomer. It is assumed that the water produced at the reaction sites diffuses through the ionomer film and reaches the agglomerate surface. There it forms a thin layer before moving out. On the other hand, oxygen that moves into the CL dissolves in the liquid water film and in the ionomer film before reaching the reaction site. The protons, generated due to the electrochemical reactions in the anode CL, move through the membrane along with water and reach the cathode CL. At the cathode CL, oxygen reacts with the protons and electrons in the presence of platinum catalyst to generate liquid water.

The following assumptions are considered for setting up the model equations:

1. Isothermal conditions are considered throughout the region of interest.
2. The contribution due to convection of species is negligible.
3. Water generated due to the reaction is in the liquid form.
4. Butler–Volmer kinetics is considered for the oxygen reduction reaction.
5. The gas mixture is assumed to behave as an ideal gas.
6. Gas diffusivities, water permeability, and electron conductivity in all the porous layers are isotropic.

The model developed in this paper is an enhancement of a previous model developed by our group [17]. The model enhancements are described below.

2.1. Water transport in the membrane

Ignoring the convection effects, water transport through the membrane is due to the electro-osmotic drag and back diffusion [16], and is given by Eq. (1):

$$N_W^{mem} = \frac{i_a}{F} n_d - D_W^{mem} \nabla C_W^{mem} \quad (1)$$

where n_d is net electro-osmotic drag coefficient, i_a is local current density ($A\,m^{-2}$), D_W^{mem} is the diffusivity of liquid water in the membrane ($m^2\,s^{-1}$), and C_W^{mem} is concentration of liquid water in the membrane (mol of $H_2O\,m^{-3}$).

At the cathode CL-membrane and anode CL-membrane interface, it is assumed that the concentration of liquid water in the membrane is in equilibrium with the water vapor activity in the gas phase [16].

At the cathode membrane interface [16]:

$$\text{If } s = 0, \quad C_w^{mem} = c_f(0.043 + 17.81\alpha_c - 39.85\alpha_c^2 + 36\alpha_c^3) \quad (2)$$

$$\text{If } s > 0, \quad C_w^{mem} = c_f(14 + 2.8s) \quad (3)$$

where c_f is the concentration of the fixed charge sites in the membrane ($mol\,m^{-3}$) and α_c is vapor activity in the gas phase in the cathode CL.

At the anode, assuming that the water exists only in the vapor form [16]:

$$C_w^{mem} = c_f(0.043 + 17.81\alpha_a - 39.85\alpha_a^2 + 36\alpha_a^3) \quad (4)$$

where α_a is vapor activity in the gas phase in the anode CL.

2.2. Proton transport in the membrane

The proton transport equation in the membrane is given by [16]:

$$-\kappa^{eff,mem} \nabla^2 \varphi_r = 0 \quad (5)$$

where $\kappa^{eff,mem}$ is the effective proton conductivity in the membrane; φ_r is the ionomer potential.

2.3. Electron transport in the cathode

The electrons generated in the anode CL travel through an external circuit to reach the cathode current collector. In the current collector, the electrical conductivity is in the range of 20,000 $S\,m^{-1}$. Hence, it is a reasonable assumption to neglect the electronic resistance in the current collector [33]. However, the effective electrical conductivity in the porous layers is low (300–500 $S\,m^{-1}$). In fact, the electrical conductivity varies both in plane and through plane directions. For model simplification purposes, we have assumed isotropic behavior. The electron transport equation in the porous layers is [16]:

$$\kappa_{ele}^{eff,k} \nabla^2 \phi_{s,k} + S_\phi = 0 \quad (6)$$

where $\kappa_{ele}^{eff,k}$ is the effective electrical conductivity in the layer k (k = GDL, MPL, CL):

$$\text{source term } (S_\phi) = 0 \text{ in GDL and MPL}$$
$$= -nFR_{O_2} \text{ in the CL}$$

The modeling equations and the boundary conditions for all the layers including the flow field and the polymer membrane are given in Tables 1 and 2 respectively.

3. Model validation

The experimental data for validating the developed model is taken from Wang et al. [22]. Experimental details are briefly given here. The experimental cell consists of a membrane electrode

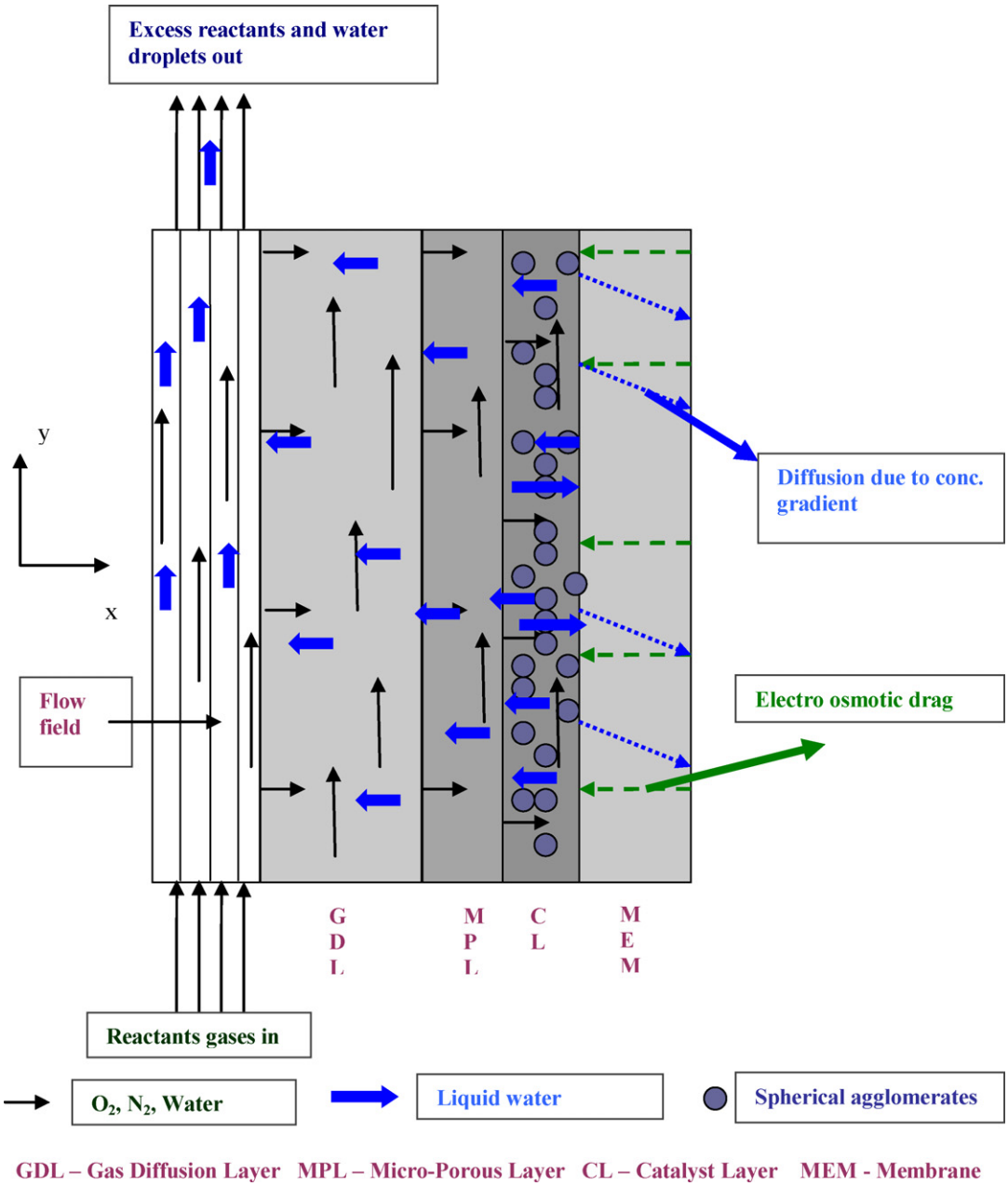

Fig. 1. Schematic of PEMFC cathode.

assembly (MEA) with a 45 μm membrane (EW < 1000). Toray carbon papers (TGP-H 090 with 20 wt% PTFE) are used for the GDL. A thin layer of MPL is coated on the GDL. The operating conditions, design parameters, model parameters, and the correlations used in this paper are given in Tables 3–6 respectively. The model is validated at two different cell operating conditions. Results of the validation study are presented in Figs. 2 and 3. To match with the experimental data, cathode exchange current density and MPL liq-

Table 1
Conservation equations (C = concentration, J, N = fluxes).

Variables	Gas channel	Diffusion layer (DL)	Microporous layer (MPL)	Catalyst layer (CL)	Polymer membrane
C_{O_2}	$-\frac{\partial}{\partial y}(C_{O_2}u) - \nabla \cdot J_{O_2} = 0$	$-\nabla \cdot (-D^{\text{eff,d}}_{O_2} \nabla C^{\text{GDL}}_{O_2}) = 0$	$-\nabla \cdot (-D^{\text{eff,m}}_{O_2} \nabla C^{\text{MPL}}_{O_2}) = 0$	$-\nabla \cdot (-D^{\text{eff,c}}_{O_2} \nabla C^{\text{CL}}_{O_2}) - R_{O_2} = 0$	–
C_{N_2}	$-\frac{\partial}{\partial y}(C_{N_2}u) - \nabla \cdot J_{N_2} = 0$	$-\nabla \cdot (-D^{\text{eff,d}}_{N_2} \nabla C^{\text{GDL}}_{N_2}) = 0$	$-\nabla \cdot (-D^{\text{eff,m}}_{N_2} \nabla C^{\text{MPL}}_{N_2}) = 0$	$-\nabla \cdot (-D^{\text{eff,c}}_{N_2} \nabla C^{\text{CL}}_{N_2}) = 0$	–
C_{H_2O}	$-\frac{\partial}{\partial y}(C_{H_2O}u) - \nabla \cdot J_{H_2O} - R_W = 0$	$-\nabla \cdot (-D^{\text{eff,d}}_{H_2O} \nabla C^{\text{GDL}}_{H_2O}) - R_W = 0$	$-\nabla \cdot (-D^{\text{eff,m}}_{H_2O} \nabla C^{\text{MPL}}_{H_2O}) - R_W = 0$	$-\nabla \cdot (-D^{\text{eff,c}}_{H_2O} \nabla C^{\text{CL}}_{H_2O}) - R_W = 0$	–
s	$-\frac{\rho_W}{M_W}\frac{\partial}{\partial y}(su) - \nabla \cdot N_{W,d} + R_W = 0$	$-\nabla \cdot N_{W,d} + R_W = 0$	$-\nabla \cdot N_{W,m} + R_W = 0$	$-\nabla \cdot N_{W,c} + R_W + 2R_{O_2} = 0$	$-\nabla \cdot N_{W,mem} = 0$
ϕ_r	–	–	–	$\kappa^{\text{eff,c}} \nabla^2\varphi_r + nFR_{O_2} = 0$	$-\kappa^{\text{eff,mem}} \nabla^2\varphi_r = 0$
ϕ_s	–	$-\kappa^{\text{eff,d}}_{\text{ele}} \nabla^2\phi_s = 0$	$-\kappa^{\text{eff,m}}_{\text{ele}} \nabla^2\phi_s = 0$	$\kappa^{\text{eff,c}}_{\text{ele}} \nabla^2\phi_s - nFR_{O_2} = 0$	

Where R_w = interfacial transfer of water between liquid and vapor phases = f (local partial pressure, local liquid saturation).
R_{O_2} is the rate of oxygen consumption.

Table 2
Boundary conditions (C = concentration, J = gaseous flux, N = liquid flux).

Variables	Entrance	GC/DL	DL/MPL	MPL/CL	CL/MEM	MEM/ANODECL
C_{O_2}	$C_{O_2} = C_{O_2,o}$	$C_{O_2}^{GC} = C_{O_2}^{DL}$	$C_{O_2}^{DL} = C_{O_2}^{MPL}$ $J_{O_2}^{DL} = J_{O_2}^{MPL}$	$C_{O_2}^{MPL} = C_{O_2}^{CL}$ $J_{O_2}^{MPL} = J_{O_2}^{CL}$	$\nabla C_{O_2}^{CL} = 0$	
C_{N_2}	$C_{N_2} = C_{N_2,o}$	$C_{N_2}^{GC} = C_{N_2}^{DL}$	$C_{N_2}^{DL} = C_{N_2}^{MPL}$ $J_{N_2}^{DL} = J_{N_2}^{MPL}$	$C_{N_2}^{MPL} = C_{N_2}^{CL}$ $J_{N_2}^{MPL} = J_{N_2}^{CL}$	$\nabla C_{N_2}^{CL} = 0$	
C_{H_2O}	$C_{H_2O} = C_{H_2O,o}$	$C_{H_2O}^{GC} = C_{H_2O}^{DL}$	$C_{H_2O}^{DL} = C_{H_2O}^{MPL}$ $J_{H_2O}^{DL} = J_{H_2O}^{MPL}$	$C_{H_2O}^{MPL} = C_{H_2O}^{CL}$ $J_{H_2O}^{MPL} = J_{H_2O}^{CL}$	$\nabla C_{H_2O}^{CL} = 0$	
s	$s = 0$	$s^{GC} = K_1 s^{DL}$	$s^{DL} = K_2 s^{MPL}$ $N_W^{DL} = N_W^{MPL}$	$s^{MPL} = K_3 s^{CL}$ $N_W^{MPL} = N_W^{CL}$	$C_W^{MEM} = C_W^{CL,EQ}(\alpha)$ $N_W^{CL} = N_W^{MEM}$	$C_W^{MEM} = C_W^{CL,EQ}(\alpha^{anode})$
ϕ_r	–	–	–	$\nabla\phi_r = 0$	$\kappa^{eff,c}\nabla\phi_{r\|CL} = \kappa^{eff,mem}\nabla\phi_{r\|MEM}$ $\phi_{r\|CL} = \phi_{r\|MEM}$	$\phi_r = 0$
ϕ_s	–	$\phi_s^{DL} = V_{cell}$	$\phi_s^{DL} = \phi_s^{MPL}$ $\kappa_{ele}^{eff,d}\nabla\phi_{s\|DL} = \kappa_{ele}^{eff,m}\nabla\phi_{s\|MPL}$	$\phi_s^{MPL} = \phi_s^{CL}$ $\kappa_{ele}^{eff,m}\nabla\phi_{s\|MPL} = \kappa_{ele}^{eff,c}\nabla\phi_{s\|CL}$	$\nabla\phi_s^{CL} = 0$	

Boundary conditions along Y-direction: fluxes of all the variables are zero at the channel entrance and exit.

uid permeability are tuned for the first data set. The second set of experimental data is validated by using the same tuning parameters. The experimental conditions for the data sets are different in terms of the operating temperature, flow rate of air, and relative humidity at the inlet of the cathode channel. Even though the model predictions are reasonably accurate in the entire range, some mismatches with the experimental data are observed. The mismatch may be due to the assumptions in the model, unconsidered mechanisms, and uncertainty in the model parameters. Beyond the current density of 1 A cm^{-2}, the experimental values of the current density are more than that predicted by the model. This mismatch may be due to the assumption of isothermal condition which may not be valid at a local level as higher amount of heat is generated at high current density. From the studies presented below, it is seen that a rise in the cell temperature (up to some value) results in a better performance of the cell. However, further model enhancements along with experimental studies are needed to verify this hypothesis.

4. Results and discussion

Even though many parametric studies are available in the literature [34–39], each study is restricted to a few parameters. Further, all the studies are either restricted to a single phase model or a two-phase model without detailed modeling of the CL. To optimize the operating conditions and the various design parameters, a detailed parametric study of all these parameters is presented with this enhanced model. In addition, a detailed study on liquid saturation is presented in this work to capture the effects of mass transfer resistance on cell performance more efficiently. To reduce the model complexity and the computational time, saturation continuity has been assumed at the interfaces for the sensitivity studies presented below.

Table 3
Cell operating conditions.

Fuel	Pure hydrogen	[22]
Oxidant	Air (21% O_2, 79% N_2)	[22]
Temperature	343.15 K	[22]
Pressure	2 atm	[22]
Air flow rate	0.505 LPM	[22]
Relative humidity	100%	[22]

Table 4
Design parameters.

Channel length	100 mm	[22]
Channel width	1 mm	[22]
Channel height	1 mm	[22]
No. of channels	7	[22]
Land width	1 mm	[22]
GDL thickness	280 μm	[22]
GDL porosity	0.7	
MPL thickness	40 μm	
MPL porosity	0.5	
CL thickness	20 μm	
CL porosity	0.112	
Platinum loading	0.4 mg cm^{-2}	[22]
Membrane thickness	45 μm	[22]
Active area of the cell	14 cm^2	[22]

4.1. Effect of operating conditions

4.1.1. Cell temperature

As the temperature increases, the exchange current density of the oxygen reduction reaction (ORR) increases due to the enhanced reaction kinetics. This reduces activation loss in the cathode. With a rise in the cell temperature, proton conductivity of the membrane increases. However, this effect is not significant at low current densities. At medium and high current densities, the effect is significant because of the reduction in ionic losses. With increase in the cell temperature, the diffusivity of the gases increases. A rise in temperature also decreases the molar concentration of oxygen for a given operating pressure. The effect of temperature on the cell performance is shown in Fig. 4. From Fig. 4, it is clear that the tem-

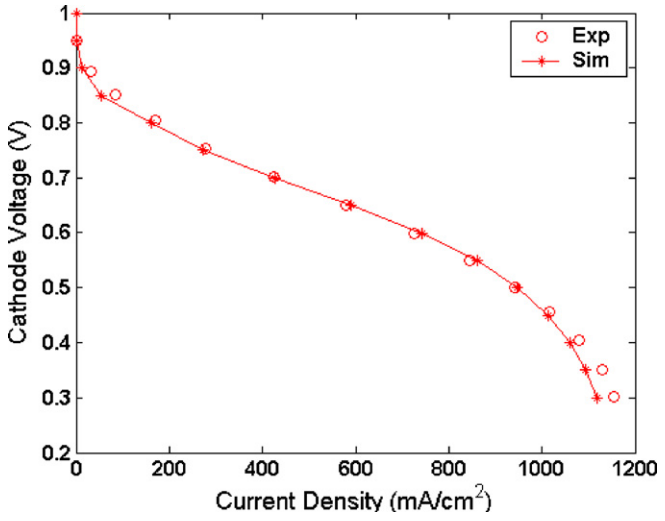

Fig. 2. Comparison of polarization curves between experimental and simulation (operating conditions: T_{cell} = 70 °C, P = 2 atm, air flow rate = 0.505 LPM, 100% RH).

Table 5
Model parameters.

Model constants			
F	96485.3	C (g equiv.)$^{-1}$	[17]
n	4		[17]
R	8.314	J mol^{-1} K^{-1}	[17]
ρ_c	1800	kg m^{-3}	[17]
ρ_{Pt}	21,450	kg m^{-3}	[17]
ρ_w	977.3	kg m^{-3}	[17]
Model parameters			
i_o	$i_0^{ref}\exp\left(-\frac{E}{R}\left(\frac{1}{T_{cell}}-\frac{1}{T_{ref}}\right)\right)$ a^{++} (a^{++} = tuning parameter)	A m^{-2} (kg Pt)$^{-1}$	[15]
E	If $V_{cell} > 0.79$	76,500 J mol^{-1}	[15]
	Else	27,700 J mol^{-1}	[15]
i_o^{ref}	If $V_{cell} > 0.79$	3.85×10^{-4} A m^{-2} (kg Pt)$^{-1}$	[15]
	Else	1.50×10^{-2} A m^{-2} (kg Pt)$^{-1}$	[15]
β	If $V_{cell} > 0.79$	1	[15]
	Else	$0.495 + 0.0023(T_{cell} - 300)$	[15]
r_{agg}	0.1	μm	[17]
$K_{wo,GDL}$	8.7×10^{-12}	m^2	[20]
$K_{wo,MPL}$	1×10^{-14}	m^2 [tuning parameter]	
$K_{wo,CL}$	3×10^{-15}	m^2	[12]
K_1	1		[17]
K_2	1		[17]
K_3	1		[17]
$-(dP_c/ds)$ in GDL	−28.42	N m^{-2}	[17]
$-(dP_c/ds)$ in MPL	−56.84	N m^{-2}	[17]
$-(dP_c/ds)$ in CL	−113.68	N m^{-2}	[17]
k_c	100	s^{-1}	[17]
k_v	100	atm^{-1} s^{-1}	[17]
κ_{ele}^{GDL}	1000	S m^{-1}	
κ_{ele}^{MPL}	1000	S m^{-1}	
$\kappa_{ele}^{eff,GDL}$, $\kappa_{ele}^{eff,MPL}$ (for model validation)	300	S m^{-1}	
κ_{ele}^{CL}	1200	S m^{-1}	
c_f	1200	mol m^{-3}	[12]

perature effect is negligible at low current densities. At medium and high current densities, the performance increases with temperature. However, the gain in performance is more from 60 to 70 °C than from 70 to 80 °C. This is due to dehydration of the membrane at high current densities under high temperatures of operation. If the cell temperature is increased above 80 °C, dehydration of the membrane becomes severe and as a result, membrane conductivity decreases and hence the performance drops. The performance curves at temperatures above 80 °C are shown in Fig. 5. At the operating temperature of 85 °C, the performance is slightly lower than at 80 °C. However, the drop in the performance is higher at 90 °C due to more ionic resistance resulting from the dehydration of the membrane. In addition, the mechanical strength of the Nafion membrane also decreases (not considered in this study) at high temperatures. In our previous work [17], the cell temperature was 65 °C at which the cell performance is not dominated by the mechanisms taking place in the polymer membrane. Therefore, ignoring the membrane did not have much impact on the model prediction. The current enhancement of the model considering the polymer membrane shows the cell performance as the mechanisms in the membrane start playing a dominating role beyond certain temperature.

4.1.2. Flow rate of air

An increase in the cathode air flow rate reduces the concentration losses and hence increases the cell performance. Since less amount of oxygen is required at low current densities, the increase in the flow rate has negligible effect on the performance at high voltage. However, as the cell produces more current, it requires

Table 6
Correlations used.

$H_{O_2}^{mem}$	$1.33\exp\left(-\frac{666}{T_{cell}}\right)$	[17]
$H_{O_2}^{W}$	$5.08\exp\left(-\frac{498}{T_{cell}}\right)$	[17]
$D_{O_2}^{mem}$	$3.1\times10^{-7}\exp\left(-\frac{2768}{T_{cell}}\right)$	[17]
a_{Pt}	$0.1(2.2779\times10^6(f_{Pt})^3 - 1.5857\times10^6(f_{Pt})^2 + 2.0153\times10^6(f_{Pt}) + 1.595\times10^6)$	[49]
a_{Pt}^{eff}	$a_{Pt}\times f_{area}$	
a_a	$a_{Pt}^{eff} m_{Pt}/t_{CL}$	
α_c	p_w/p^{sat}	
C_W^{mem}	If $s=0$, $c_f(0.043 + 17.81\alpha_c - 39.85\alpha_c^2 + 36\alpha_c^3)$	[16]
	If $s>0$, $c_f(14.0 + 2.8s)$	[16]
λ_w	C_w^{mem}/c_f	[16]
n_d	$2.5\lambda_w/22$	[16]
κ^{eff}	$100(0.005139\lambda_w - 0.00326)\exp\left(1268\left(\frac{1}{303}-\frac{1}{T_{cell}}\right)\right)$	
D_W^{mem}	For $\lambda_w > 4$, $10^{-10}(2.563 - 0.33\lambda_w + 0.0264\lambda_w^2 - 0.000671\lambda_w^3)\exp\left(2416\left(\frac{1}{303}-\frac{1}{T_{cell}}\right)\right)$	
	$3 < \lambda_w \le 4$, $10^{-10}(6.89 - 1.33\lambda_w)\exp\left(2416\left(\frac{1}{303}-\frac{1}{T_{cell}}\right)\right)$	[16]
	$2 < \lambda_w \le 3$, $10^{-10}(-3.1 + 2.0\lambda_w)\exp\left(2416\left(\frac{1}{303}-\frac{1}{T_{cell}}\right)\right)$	

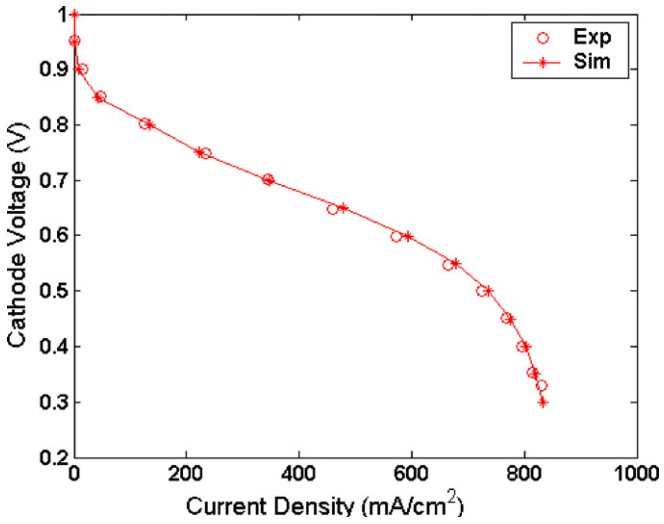

Fig. 3. Comparison of polarization curves between experimental and simulation (operating conditions: T_{cell} = 62 °C, P = 2 atm, air flow rate = 0.256 LPM, 150% RH).

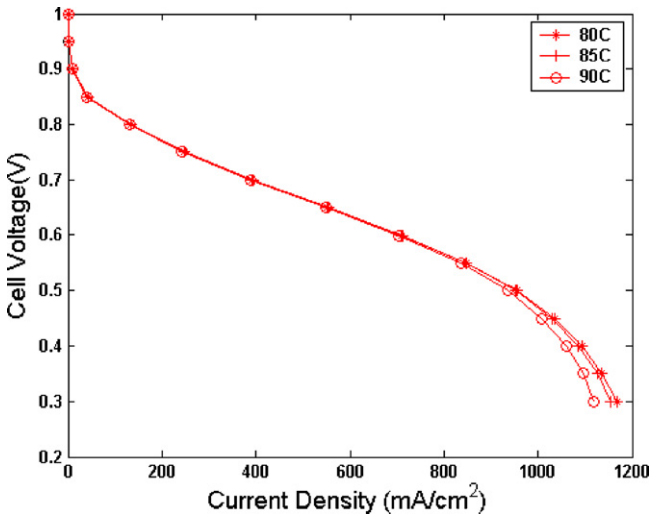

Fig. 5. Cell performance at high temperatures of operation.

larger amount of oxygen. The increase in the flow rate not only supplies required amount of oxygen for the cathode reduction reaction but also increases the catalyst utilization. The effect of air flow rate on the cell performance is studied by keeping the cathode pressure constant. In this study, the pressure drop through the channel has been considered negligible irrespective of the flow rate. This may not be true if the flow rate is increased beyond a high value. Therefore, this study is done by changing the flow rate in a small range where the pressure drop across the channel can be considered negligible. The results are shown in Fig. 6. When the flow rate is increased from 0.2 to 0.5 LPM, a substantial rise in the cell performance is observed especially at high current densities. The improvement in the performance is comparatively less when the flow rate of air is increased from 0.5 to 1 LPM. This study suggests that there is a flow rate beyond which an increase in the flow rate will have no effect on the cell performance.

4.2. Diffusion layer design parameters

4.2.1. Porosity of the diffusion medium

The diffusion medium plays a key role in the transport of the reactants to the reaction sites and liquid water from the reaction sites. An increase in the porosity of the diffusion layers decreases the concentration losses. On the other hand, the ohmic loss increases with increase in porosity. However, the ohmic loss is relatively less (due to high electric conductivity of the GDL) than the concentration loss till a very high value of porosity is reached. The effect of change in the void fractions of the GDL is shown in Fig. 7. From the figure, it is observed that the increase in porosity from 0.5 to 0.7 results in better performance at high current densities. But as the porosity is increased to 0.8, the ohmic losses dominate and the performance decreases. The study suggests that the optimum porosity of the GDL for this cell is 0.7–0.8. Similar effects are observed for the MPL too.

4.3. Catalyst layer design parameters

4.3.1. Effect of platinum loading

With the increase in platinum loading, the effective area of platinum per unit volume of the reaction layer increases and hence, the rate of oxygen reduction reaction increases. It also results in an increase of the solids (platinum and carbon) and membrane fractions and a decrease in the void fraction. As a result of this, electric and ionic resistances decrease and the mass transfer resistance increases. To study the effect of platinum loading on the cell performance, simulations are performed at various platinum loadings in the range of 0.2–0.45 mg cm^{-2} and the results are shown

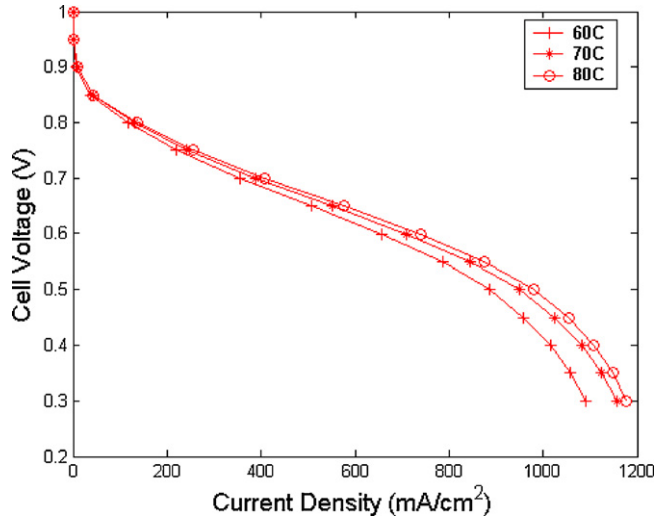

Fig. 4. Effect of cell temperature on performance.

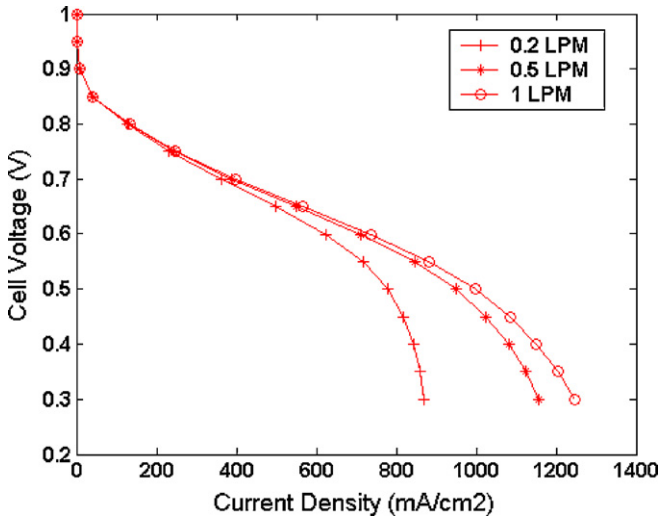

Fig. 6. Performance curves at different air flow rates.

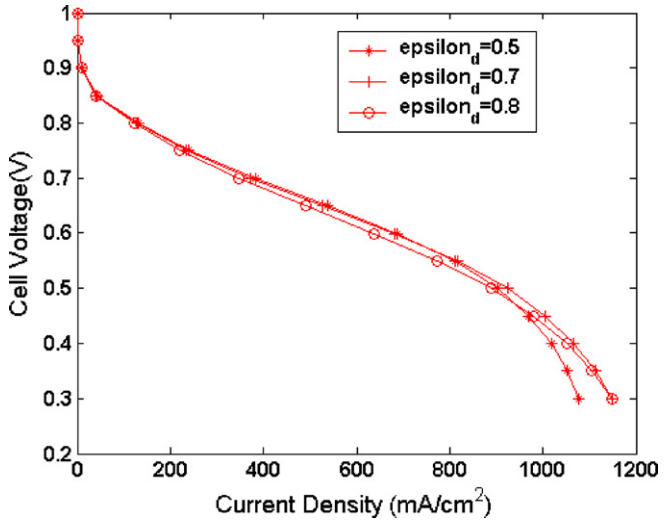

Fig. 7. Effect of GDL porosity on the cell performance.

in Fig. 8. A significant rise in the cell performance is observed in the entire operating range when the platinum loading is increased from 0.2 to 0.25 mg cm^{-2}. When the platinum loading is increased to 0.35 mg cm^{-2}, a small rise in the cell performance is observed because of the increase in mass transfer resistance. Further increase in the platinum loading results in a significant decrease in the performance due to severe mass transfer resistance. The effect of platinum loading on cell power density is shown at low and high current densities in Fig. 9. At low current density (at a cell potential of 0.85 V), the power increases monotonically with the platinum loading. However, at high current density, the power first increases up to certain platinum loading and then decreases. From these plots, it is observed that there is an optimum platinum loading at each operating voltage which gives the maximum cell performance. The optimum loading of platinum for this cell is about 0.3–0.4 mg cm^{-2}. However, this optimum loading is expected to change with operating conditions and also with the other design parameters of the cell.

4.3.2. Catalyst layer thickness

Usually, the thickness of a cathode CL is in the range of 10–30 μm. As the thickness is increased, the effective area of platinum per unit volume of the catalyst layer decreases. As a result,

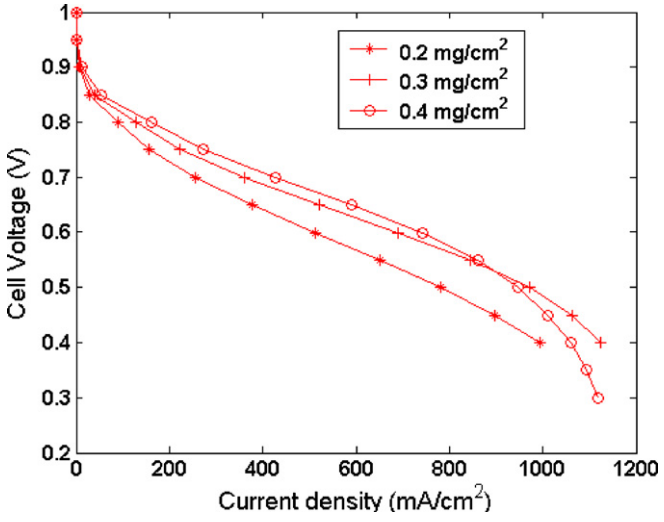

Fig. 8. Performance curves at various platinum loadings (f_{Pt} = 0.2, f(ionomer) = 0.35, CL thickness = 15 μm).

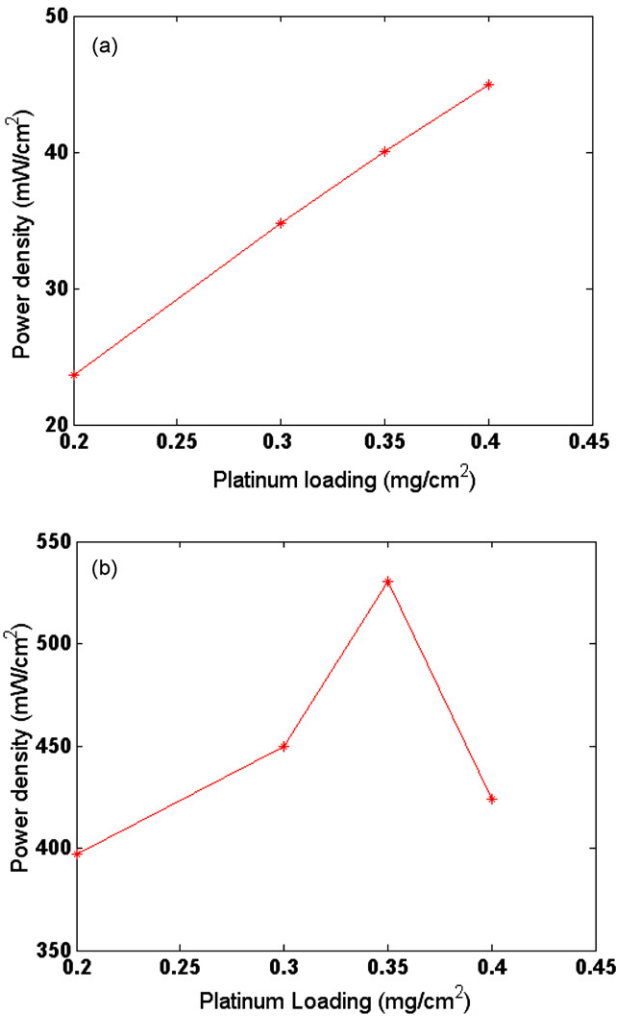

Fig. 9. Cell power density for different platinum loadings at (a) 0.85 V and (b) 0.4 V.

the oxygen consumption also decreases. Since the volumes of the ionomer and carbon/platinum are constant, and there is an increase in the volume of the reaction layer, the volume fraction of both the ionomer and solids decreases. This results in a reduction of proton and electron conductivities. On the other hand, with the increase in the reaction layer thickness, the void fraction increases. Hence, mass transfer losses decrease. However, an increase in the thickness increases the diffusion path length. The effect of the reaction layer thickness on the overall performance is shown in Fig. 10. The cell performance is reduced when the thickness of the CL is increased from 10 to 15 μm at low and medium current densities. Due to the dominant effect of high diffusivity of oxygen, a rise in performance is observed at high current densities. Further increase in the thickness causes a fall in the performance throughout the polarization range due to the combined effect of the ionic, electric, and mass transfer resistances.

4.3.3. Fraction of ionomer

An increase in ionomer fraction results in lesser porosity and lesser ionic loss. As a result, mass transfer resistance increases. Since, mass transfer losses are higher at high current densities, increase of ionomer fraction results in larger concentration overpotential. The ionomer fraction has no effect on the solid fraction and hence the electric losses remain the same. The performance curves for various ionomer fractions are shown in Fig. 11. It is observed that high ionomer fractions provide more current at high operating voltages. At medium and low operating voltages, the current

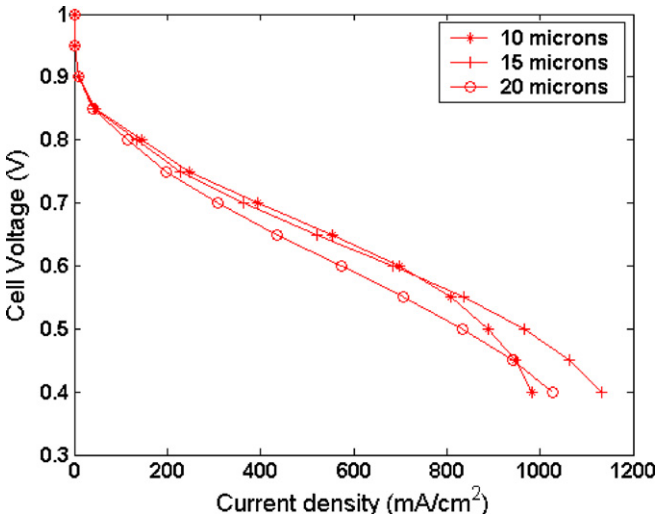

Fig. 10. Effect of CL thickness on cell performance (f(Pt/C) = 0.2, f(ionomer) = 0.35, platinum loading = 0.4 mg cm^{-2}).

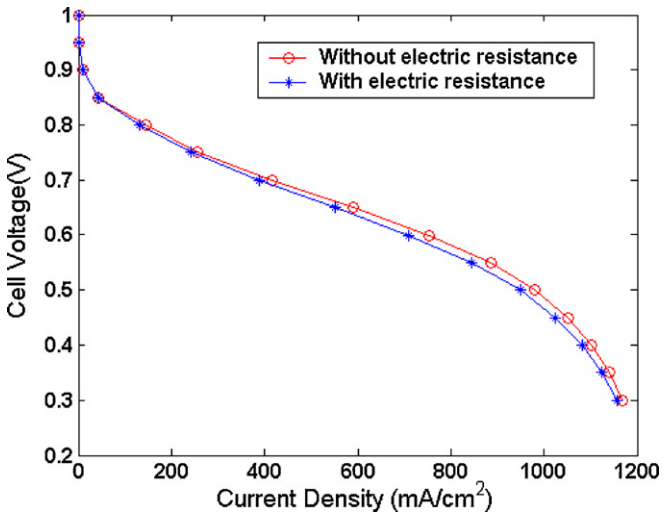

Fig. 12. Cell performance as predicted by the models with and without electric resistance.

produced first increases and then decreases with an increase in the ionomer loading.

A summary of the studies presented above is given in Tables 7 and 8. The effects of CL design parameters on various resistances are summarized in Table 7. The optimum range of design parameters at different operating voltages is given in Table 8. In this study, one variable is varied at a time by keeping the others constant. From the CL parametric study, it is observed that an optimum combination of the design parameters exists at each operating voltage.

4.4. Model parameters

4.4.1. Effect of electric conductivity

In most of the models, it is assumed that the electric resistance is negligible to make the model simpler. In Table 7, we have shown the role of electric resistance of the CL on the performance of the cell. Similarly, there is a drop in the voltage due to the electrical resistance in the diffusion medium. A detailed study of the electron transport in PEFCs can be found in the work of Meng and Wang [33]. As the thickness of the GDL increases, the electronic resistance increases. A similar effect can be observed in the MPL also. In the literature, a range of values can be found for the electric conductivity of the cathode materials. However, the effective conductivities are typically 300–500 S m^{-1}. The cell performance with and without electric resistance is shown in Fig. 12. With the current design parameters, operating conditions, and materials of construction, the ohmic loss is not very significant. In particular, the electric loss is negligible below a current density of 500 mA cm^{-2} which is the maximum current density in our previous model [17]. So neglecting that loss did not have much impact on the results of our previous model. However, if the design parameters and operating conditions are altered in a sensitivity study or during optimization, the ohmic loss can increase significantly and the model should be capable of capturing it precisely. The effect of the effective electric conductivity of the diffusion medium on cell performance is shown in Fig. 13. At very low electric conductivities, the performance decreases significantly due to very high electric resistance.

4.5. Water management study

Water management is a critical issue in PEMFCs. Excessive water causes flooding which results in high mass transfer resistance. On the other hand, lack of adequate water results in drying which

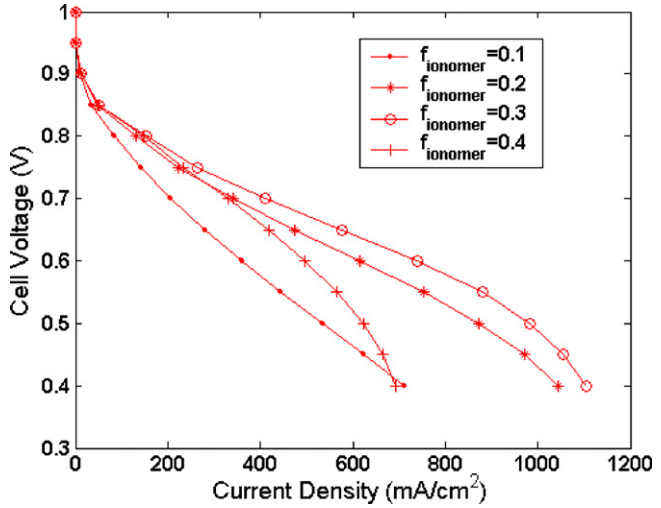

Fig. 11. Performance curves at various ionomer fractions (f(Pt/C) = 0.2, platinum loading 0.4 mg cm^{-2}, CL thickness = 15 μm).

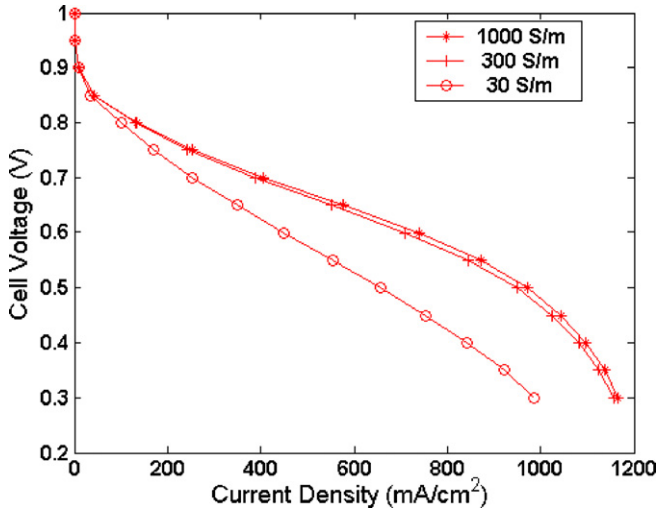

Fig. 13. Effect of diffusion medium effective electric conductivity on cell performance.

Table 7
The effects of CL design parameters on various resistances.

Design variable (with increase)	Effective mass transfer diffusivity	Electronic resistance	Ionic resistance	Effective area of the catalyst per unit volume of reaction layer
Platinum loading	Decreases	Decreases	Decreases	Increases
Reaction layer thickness	Increases	Increases	Increases	Decreases
f(ionomer)	Decreases	No change	Decreases	No change

Table 8
Optimum operating range of catalyst layer design parameters.

Cell voltage (V)	Platinum loading (mg cm^{-2})	Catalyst layer thickness (μm)	f(ionomer)
0.8	0.40–0.45	10–15	0.25–0.40
0.6	0.35–0.40	10–15	0.25–0.30
0.4	0.30–0.35	10–20	0.25–0.30

increases the ionic resistance. To minimize these losses, proper water content should be maintained. The humidified gases carry water vapor on both sides of the cell. In addition to this, a significant amount of liquid water is generated on the cathode side due to the electrochemical reaction. The liquid water flows from the CL to the GDL – gas channel interface through the open pores by capillary pressure gradient. It is important to maintain a capillary pressure gradient for effective removal of the liquid water from the cell without flooding or drying the cell. Various correlations are available to calculate the capillary pressure [31,32,40]. Pasaogullari and Wang [19] calculated the capillary pressure using Leverette and Udell [40] function:

$$P_c = \sigma \cos(\theta_c)\left(\frac{\varepsilon}{K}\right)^{0.5} J(s) \quad (7)$$

where $J(s)$ is Leverette function which is defined as

$$1.417s - 2.120s^2 + 1.263s^3$$

for a hydrophobic medium ($90^\circ < \theta_c < 180^\circ$)

$$1.417(1-s) - 2.120(1-s)^2 + 1.263(1-s)^3$$

for a hydrophilic medium ($0^\circ < \theta_c < 90^\circ$)

The contact angle θ_c is dependent upon PTFE content of the medium.

Other expressions used to calculate the capillary pressure are

- Van Genuchten [41]:

$$P_c = p_d[(1-s)^{-1/m} - 1]^{1-m} \quad (8)$$

- Brooks–Corey [42]:

$$P_c = p_d(1-s)^{-1/h} \quad (9)$$

where p_d is the entry pressure required to displace the wetting phase from the largest pore of the medium. The parameters m and h are Van Genuchten and Brooks–Corey parameters respectively. One of the usual boundary conditions used in these studies is the continuity of capillary pressure at the interface.

Ye and Nguyen [31] have experimentally measured capillary pressures in the porous transport layer [PTL] and catalyst layer [CL]. They have developed the following empirical expression (Eq. (10)) to calculate the capillary pressure as a function of liquid saturation from the experimental data:

$$P_c = (e^{-a1(s-c)} - e^{a2(s-c)})d + b \quad (10)$$

The coefficients $a1$ and $a2$ account for symmetry of the capillary functions. The coefficients $a1$, $a2$, b, c, and d are different for the PTL and the CL. The authors have simulated the liquid water distribution through a single domain approach. Due to this, the interface boundary conditions are not explicitly mentioned. Considering a Toray TGP-H-060 carbon paper with 10% PTFE, their study shows that the capillary pressure decreases steeply around a liquid saturation of 0.05–0.1. After that, the capillary pressure does not change significantly till a saturation of 0.4. After that, it becomes negative and changes steeply. These results are in qualitative agreement with the experimental work of Fairweather et al. [43] and Gallgher et al. [44]. The works of Fairweather et al. [43] and Gallgher et al. [44] show that the P_c vs. s depends not only on the material, but also on the wetting history. The P_c vs. s correlation can be significantly different based on whether the medium is imbibing or draining.

Change in the value of the capillary pressure with the liquid saturation as predicted by Eqs. (7), (8), and (10) is shown in Fig. 14. The parameters such as void fraction, permeability, etc. used in the calculation of capillary pressure for various correlations are given in Table 9. The operating conditions and the capillary pressure related parameters that are used in this part of study are different from those used in the parametric study. High flow rate, temperature, and permeability values are used to study the effects of MPL and the role of saturation. Eq. (10) shows that the P_c changes from a positive value to a negative value as the saturation is increased. On the other hand, Eqs. (7) and (8) show a negative value irrespective of the saturation. Capillary pressure gradients with saturation are shown in Figs. 15–17. From these figures, it is observed that each correlation gives a completely different picture of the gradients.

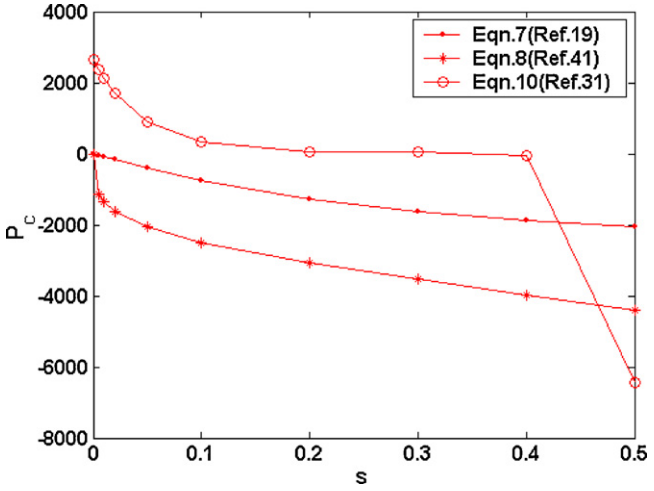

Fig. 14. P_c vs. s in GDL for various correlations.

Table 9
Parameters used in capillary pressure calculation.

Correlation	Parameters	GDL	MPL	CL
Pasaogullari and Wang [19,40]	(ε)	0.7	0.5	0.2850
	(θ)	110	120	100
	(K) m^2	8.7×10^{-12}	3×10^{-14}	9×10^{-15}
Van Genuchten [32,41]	(P_d) Pa	-4×10^3	-6×10^3	-2×10^3
	($\theta = 110^\circ$)	($\theta = 120^\circ$)	($\theta = 100^\circ$)	
	m	0.75	0.75	0.75
Ye and Nguyen [31]	GDL and CL parameters are taken from Ref. [31]			

Table 10
Order of dP_c/ds with s for various correlations.

s	Pasaogullari and Wang [19,40]			Van Genutchen [32,41]			Qe and Nguyen [31]		
	GDL	MPL	CL	GDL	MPL	CL	GDL	MPL	CL
	Order (to the power 10)			Order (to the power 10)			Order (to the power 10)		
0	3	5	4				4	NA	1
0.1	3	5	4	3	4	3	3	NA	1
0.2	3	5	4	3	3	3	2	NA	1
0.3	3	4	4	3	3	3	2	NA	1
0.4	3	4	4	3	3	3	3	NA	1
0.5	3	4	4	3	3	3	5	NA	2
0.6	3	4	4	3	3	3	7	NA	6
0.7	3	4	4	3	4	3	9	NA	10
0.8	3	4	4	4	4	3	11	NA	14
0.9	3	4	4	4	4	4	13	NA	18
1	3	5	4	5 (at $s = 0.99$)	5 (at $s = 0.99$)	5 (at $s = 0.99$)	15	NA	22

From Fig. 15, it is observed that there is a significant difference in the capillary gradients between all the layers at low saturations (0–0.25) and at very high saturations (0.8–1.0). A peak value in the gradient is observed at a saturation of 0.6 in all the layers. Compared to the MPL and CL, the change in the gradient is low in the GDL. Capillary pressure gradients calculated from Eq. (8) are shown in Fig. 16. A sharp decrease in the gradient is observed at very low concentrations and a uniform decrease till the saturation of 0.9. As the saturation approaches unity, the gradient becomes infinity. All the porous layers followed the same trend in the capillary pressure gradient with s throughout the saturation range using Eqs. (7) and (8) (Figs. 15 and 16). In the work of Ye and Nguyen [31], the capillary pressure gradient showed similar trend in the GDL and CL only after a saturation of 0.5. Till that saturation, the gradient is almost constant in the CL and a monotonic decrease is observed in the GDL. The common characteristic of Figs. 15 and 16 is that the capillary pressure gradient is more in the MPL than the GDL and CL throughout the saturation. The orders of the gradient with saturation for all correlations are shown in Table 10.

From the discussion above, it is seen that considerable disagreement exists between researchers about the correlation that can be used for accurate results. Further experiments with different materials and varied PTFE content should be done in a broad operating region to check the validity of the correlation developed. For simplicity, the capillary pressure gradient with saturation is assumed constant in this paper for all the porous layers in this operating range and for the given surface wettabilities. A similar approach has been adopted by Lin et al. [12], Lin and Nguyen [16] and Rao et al. [17].

From the assumption of constant capillary pressure gradients, it can be said that capillary pressure is a linear function of liquid satu-

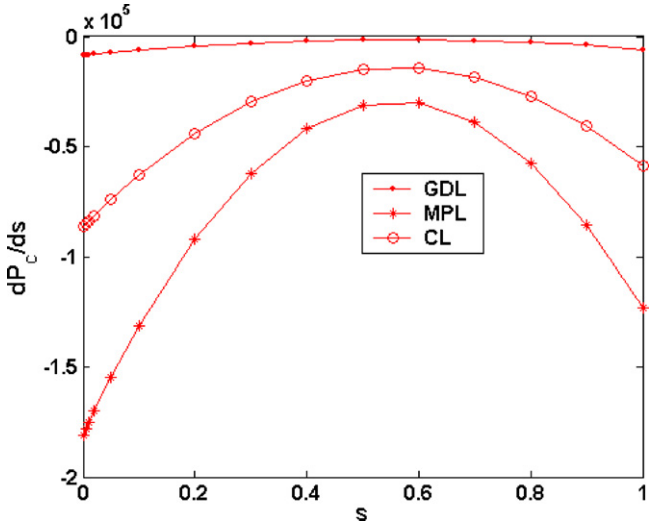

Fig. 15. dP_c/ds vs. s from Eq. (7) [19,40].

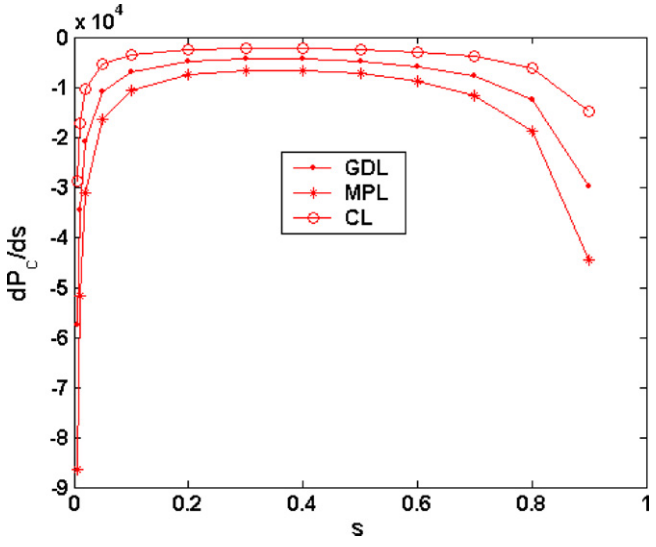

Fig. 16. dP_c/ds vs. s from Eq. (8) [32,41].

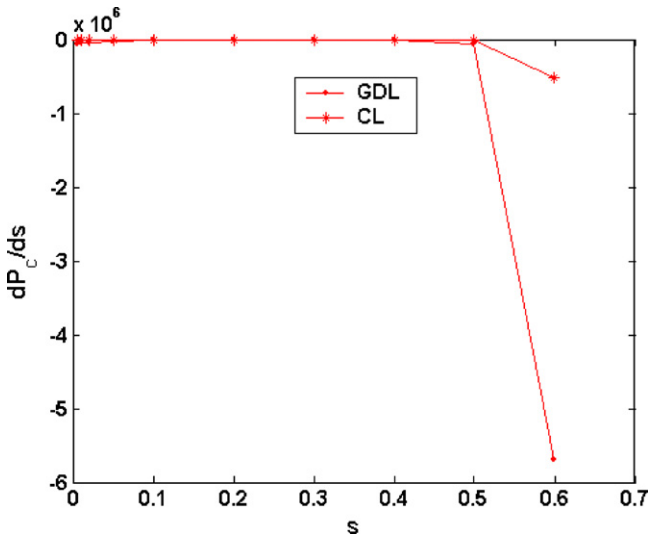

Fig. 17. dP_c/ds vs. s from Eq. (10) [31].

ration(s) in all the layers and with the assumption that the capillary pressure is continuous at the interfaces for all feasible combinations of saturations, the following relations are developed at the interfaces in terms of liquid saturations:

$$s_{GDL} = \left(\frac{c_2}{c_1}\right) s_{MPL} \quad (11)$$

$$s_{MPL} = \left(\frac{c_3}{c_2}\right) s_{CL} \quad (12)$$

As the capillary pressure has been assumed to be a linear function of the saturation, the values of the constants in Eqs. (11) and (12) can be strong function of the pore size, porosity, and hydrophobicity of the interfacing layers. Depending on these, the saturation discontinuity at the interface can show different behavior. A few computational and experimental studies exist in the open literature that has looked into the interaction of the MPL with other layers of the cell. In the work of Newman and Weber [45], the saturation is found to increase at the cathode CL/MPL interface towards the MPL side. A reverse profile is reported in the work of Meng [46] and Wang and Nguyen [47]). In the experimental study of Ramasamy et al. [48], a PEMFC comprising Carbel carbon cloth coated with MP30z microlayer is found to perform a little better under wet condition than a PEMFC with bare Carbel carbon cloth in the low and medium current density region, whereas the performance of the cell with the MPL is considerably lower in the high current density region than the bare cell. A completely reverse performance is observed when the same GDL is coated with a different MPL. The complicated interaction between the MPL and other layers in the cell shows that the constants in Eqs. (11) and (12) can have different values for different materials and design parameters. In this work, a study was done by considering the following values: $c_2/c_1 = 1.5$, $c_3/c_2 = 4/1.5$, $K_{wo,GDL} = 8.7 \times 10^{-12}$ m^2, $K_{wo,MPL} = 3 \times 10^{-14}$ m^2 and $K_{wo,CL} = 9 \times 10^{-15}$ m^2. The results are shown in Table 11. An insignificant improvement in the cell performance is observed in the presence of a MPL in the low and medium current density region whereas the cell without MPL performs better in the high current density region. The results are similar to the experimental results of Ramasamy et al. [48] for a PEMFC comprising Carbel carbon cloth coated with MP30z microlayer under wet condition as mentioned earlier. The study shows that for certain combination of materials and for some operating conditions, the presence of a MPL can lower the performance of a PEMFC. To take full advantage of the MPL, the mechanism by which a MPL interacts with other layers and its role under different operating conditions need to be clearly understood. This requires further computational and experimental investigations.

Table 11
Performance comparison with and without MPL for $c_2/c_1 = 2$ and $c_3/c_2 = 2$ (with MPL) and $c_3/c_1 = 4$ (without MPL) (the higher current density is shown in bold).

Voltage (V)	Current density (mA cm^{-2})	
	With MPL	Without MPL
1	**1.6278**	1.6243
0.95	**8.1238**	8.0948
0.9	**35.787**	35.593
0.85	**116.71**	115.82
0.8	**267.7**	264.73
0.75	**449.77**	443.42
0.7	**647.37**	637.08
0.65	**867.8**	853.51
0.6	**1101**	1084.3
0.55	**1336.7**	1321.7
0.5	**1565.1**	1558.9
0.45	1777.6	**1789.8**
0.4	1967.4	**2009.5**

5. Conclusions

An enhanced model of a PEMFC cathode is developed for sensitivity and optimization studies by incorporating new mechanisms to a previously published model [17]. Transport of water and proton through the polymer membrane is considered. In addition, transport of electrons through all the layers in the cathode is also modeled. The additional loss mechanisms considered in this paper may be insignificant in a particular operating condition for a particular cell. But, these losses can be considerable as the current density from the cell increases, the operating condition changes, and the design parameters deviates a lot from the base case condition as the search space is widened during an optimization study. As an example, the study shows that the electric loss is negligible below a current density of 500 mA cm^{-2} for this cell. In another study, it is seen that if the cell temperature is increased above 80 °C, dehydration of the membrane becomes severe and as a result, membrane conductivity decreases and hence the performance drops. As observed in these two examples, the model enhancement helped to capture the cell performance as the operating conditions and design parameters deviated from the base case conditions.

While validating the model with experimental data, a mismatch is observed between the results of the model and the experimental data beyond a current density of 1 A cm^{-2}. The mismatch may be because of the implicit and explicit assumptions in the model, unconsidered mechanisms that may play a key role under certain circumstances, and uncertainty in the model parameters, both estimated and taken from the literature. Based on the observations, further enhancement of the model will be done in future.

The study on operating conditions showed that the optimum operating temperature of the cell is 80–85 °C and the performance of the cell is better at high flow rates. This study shows that there is a flow rate beyond which an increase in the flow rate will have negligible effect on the cell performance. Issues such as parasitic losses and utilization factor should also be considered for a better estimate of the optimum flow rate for a cell. The study suggests that the optimum porosity of the GDL for this cell is in the range of 0.7–0.8. A study is conducted by varying three key design parameters of the CL – platinum loading, thickness of the CL, and fraction of ionomer. Each parameter is varied at a time by keeping others constant. The study suggests that a thin CL with about 0.4–0.45 mg cm^{-2} platinum loading and 25–40 wt% of ionomer provides good performance at low current densities (up to about 0.2 A cm^{-2}). At high

current densities, for example at 1 A cm^{-2}, the cell performs better with 0.3–0.35 mg cm^{-2} of platinum and 25–30 wt% of ionomer loading. Change in the capillary pressure with liquid saturation is calculated considering various correlations available in the open literature. Wide differences are observed in the calculated values. For simplicity, a constant value of dP_c/ds is assumed in all the layers. By equating the capillary pressures at various interfaces, a linear relation for interfacial saturation is developed. A study is done by varying the value of dP_c/ds in all the layers. The study shows that under certain operating conditions and for certain combination of materials in the GDL and CL, presence of a MPL can actually deteriorate the performance. This warrants further computational and experimental investigations for better understanding of the mechanism by which a MPL interacts with other layers of a cell. The sensitivity studies in this work have been done by varying one variable at a time. For the optimum combination of the design parameters, a multi-variable optimization study is being conducted with the developed model.

Acknowledgements

We would like to acknowledge American Chemical Society-Petroleum Research Fund (ACS-PRF) for providing partial financial support for this work through Grant#PRF 42842-AC9.

References

[1] T.E. Springer, T.A. Zawodzinski, S. Gottesfeld, J. Electrochem. Soc. 138 (8) (1991) 2334–2342.
[2] D.M. Bernardi, M.W. Verbrugge, AIChE J. 37 (8) (1991) 1151–1163.
[3] D.M. Bernardi, M.W. Verbrugge, J. Electrochem. Soc. 139 (9) (1992) 2477–2491.
[4] T.V. Nguyen, R.E. White, J. Electrochem. Soc. 140 (8) (1993) 2178–2186.
[5] P. Cheng, C.Y. Wang, Int. J. Heat Mass Transfer 39 (17) (1996) 3619–3632.
[6] V. Gurav, H. Liu, S. Kakac, AIChE J. 44 (11) (1998) 2410–2422.
[7] S. Um, C.Y. Wang, K.S. Chen, J. Electrochem. Soc. 147 (12) (2000) 4485–4493.
[8] W. He, J.S. Yi, T.V. Nguyen, AIChE J. 46 (10) (2000) 2053–2064.
[9] K. Dannenberg, P. Ekdunge, G. Lindbergh, J. Appl. Electrochem. 30 (2000) 1377–1387.
[10] D. Natarajan, T.V. Nguyen, J. Electrochem. Soc. 148 (12) (2001) A1324–A1335.
[11] T. Berning, N. Djilali, J. Electrochem. Soc. 150 (12) (2003) A1589–A1598.
[12] G. Lin, W. He, T.V. Nguyen, J. Electrochem. Soc. 151 (12) (2004) A1999–A2006.
[13] J. Fimrite, H. Struchtrup, N. Djilali, J. Electrochem. Soc. 152 (9) (2005) A1804–A1814.
[14] B.R. Sivertsen, N. Djilali, J. Power Sources 141 (2005) 65–78.
[15] W. Sun, B.A. Peppley, K. Karan, Electrochim. Acta 50 (2005) 3359–3374.
[16] G. Lin, T.V. Nguyen, J. Electrochem. Soc. 153 (2) (2006) A372–A382.
[17] R.M. Rao, D. Bhattacharyya, R. Rengaswamy, S.R. Choudhury, J. Power Sources 173 (2007) 375–393.
[18] Qi. Zhigang, A. Kaufman, J. Power Sources 109 (2002) 38–46.
[19] U. Pasaogullari, C.Y. Wang, Electrochim. Acta 49 (2004) 4359–4369.
[20] U. Pasaogullari, C.Y. Wang, K.S. Chen, IMECE04 Proceedings, 2004, pp. 1–9.
[21] A.Z. Weber, J. Newmann, J. Electrochem. Soc. 152 (4) (2005) A677–A688.
[22] X.G. Wang, F.Y. Zhang, A.L. Lubawy, C.Y. Wang, Electrochem. Solid-State Lett. 7 (11) (2004) A408–A411.
[23] U. Pasaogullari, C.Y. Wang, J. Electrochem. Soc. 151 (3) (2004) A399–A406.
[24] F.Y. Zhang, X.G. Wang, C.Y. Wang, J. Electrochem. Soc. 153 (2) (2006) A225–A232.
[25] S. Um, C.Y. Wang, J. Power Sources 125 (2004) 40–51.
[26] G.J.M. Janssen, J. Electrochem. Soc. 148 (12) (2001) A1313–A1323.
[27] A.Z. Weber, J. Newmann, AIChE J. 50 (12) (2004) 3215–3226.
[28] Q. Van, H. Toghiani, J. Wu, J. Power Sources 158 (2006) 316–325.
[29] F. Liu, G. Lu, C.Y. Wang, J. Membr. Sci. 287 (2007) 126–131.
[30] M. Acosta, C. Merten, G. Eigenberger, H. Class, R. Helmig, B. Thoben, H. Muller-Steinhagen, J. Power Sources 159 (2006) 1123–1141.
[31] Q. Ye, T.V. Nguyen, J. Electrochem. Soc. 154 (12) (2007) B1242–B1251.
[32] J. Hermann, C. Ziegler, J. Electrochem. Soc. 155 (10) (2008) B1066–B1076.
[33] H. Meng, C.Y. Wang, J. Electrochem. Soc. 151 (2004) A358–A367.
[34] L. Wang, A. Hussar, T. Zhou, H. Liu, J. Hydrogen Energy 28 (2003) 1263–1272.
[35] T. Berning, N. Djilali, J. Power Sources 124 (2003) 440–452.
[36] A. Kazim, P. Forges, H.T. Liu, Int. J. Energy Res. 27 (2003) 401–414.
[37] H. Sun, H. Liu, L.J. Guo, J. Power Sources 143 (2005) 125–135.
[38] W. Sun, B.A. Peppley, K. Karan, J. Power Sources 144 (2005) 42–53.
[39] P.K. Das, X. Li, Z.S. Liu, J. Electroanal. Chem. 604 (2007) 72–90.
[40] K.S. Udell, Int. J. Heat Mass Transfer 28 (1985) 285–495.
[41] M.T. Van Genuchten, Soil Sci. Soc. Am. J. 44 (1980) 892–898.
[42] R.J. Brooks, A.T. Corey, Hydraulic Properties of Porous Media, Hydraulic Paper 3, Colorado State University, Fort Collins, CO, 1964.
[43] J.D. Fairweather, P. Cheung, J. St-Pierre, D.T. Schwartz, Electrochem. Commun. 9 (2007) 2340–2345.
[44] K.G. Gallgher, R.M. Darling, T.W. Patterson, M.L. Perry, J. Electrochem. Soc. 155 (11) (2008) B1225–B1231.
[45] A.Z. Weber, J. Newman, J. Electrochem. Soc. 152 (4) (2005) A677–A688.
[46] H. Meng, Int. J. Hydrogen Energy 34 (2009) 5488–5497.
[47] X. Wang, T. Nguyen, ECS Trans. 16 (2) (2008) 3–12.
[48] R.P. Ramasamy, E.C. Kumbur, M.M. Mench, W. Liu, D. Moore, M. Murthy, Int. J. Hydrogen Energy 33 (2008) 3351–3367.
[49] M. Secanell, K. Karan, A. Suleman, N. Djilali, Electrochim. Acta 52 (2007) 6318–6337.